Highly Sensitive MXene/Si X-ray Detector via Graphene Interfacial Engineering

Yance Chen[1,2#], Xuan Ye[1,2#], Muhammad Abid Anwar[1#], Xin Ming[2], Wenbo Zhao[1,2], Jian Chai[1], Xiaochen Wang[1], Yunfei Xie[1], Wenzhang Fang[1]*, Srikrishna Chanakya Bodepudi[1]*, *Member, IEEE*, Chao Gao[2]*, Yang Xu[1]*, *Senior Member, IEEE*

1 College of Integrated Circuits, ZJU-Hangzhou Global Scientific and Technological Innovation Center, State Key Laboratory of Silicon and Advanced SemiconductorMaterials, Zhejiang University, Hangzhou, China

2 MOE Key Laboratory of Macromolecular Synthesis and Functionalization, Department of Polymer Science and Engineering, International Research Center for X Polymers, Zhejiang University, Hangzhou, China. *Email: wenzhang.fang@zju.edu.cn, bodepudi@zju.edu.cn, chaogao@zju.edu.cn, yangxu-isee@zju.edu.cn

[#]These authors contributed equally: Yance Chen, Xuan Ye, Muhammad Abid Anwar

***Abstract*—Developing compact, low-dose X-ray detectors demands novel material integration strategies to enhance sensitivity and scalability. While emerging materials like MXenes offer advantages over conventional perovskites in environmental stability and carrier transport, their interfacial dynamics with semiconductors remain a critical performance bottleneck. Here, we report a $Ti_3C_2T_x$ MXene/Si X-ray detector with a graphene-engineered heterointerface that achieves outstanding performance metrics. By inserting a monolayer graphene between MXene and silicon, we suppress dark current by two orders of magnitude while doubling photocurrent under X-ray irradiation (20 keV, 1.62 $\mu Gy_{air}\ s^{-1}$), yielding a record sensitivity of $2.5 \times 10^6\ \mu C\ Gy_{air}^{-1}\ cm^{-2}$. The optimized device demonstrates ultra-low noise spectral density ($1.6 \times 10^{-26}\ A^2 \cdot Hz^{-1}$) and limit of detection (1.27 $nGy_{air}\ s^{-1}$), and rapid response speed (38 µs). Leveraging a single-pixel imaging system with Hadamard modulation and iterative reconstruction algorithms (ISTA), we validate high-resolution radiography capabilities. Crucially, the van der Waals-integrated MXene/graphene/Si architecture, enabling scalable fabrication with low-dose and high-speed X-ray detection. This interfacial engineering strategy addresses key challenges in hybrid X-ray detection and establishes a universal framework for integrating 2D materials with CMOS-compatible platforms, advancing next-generation medical, security, and industrial imaging technologies.**

Keywords*—X-ray, MXene, Graphene, Silicon, Interfacial engineering

I. Introduction

Compact and ultrafast X-ray detectors are crucial for emerging medical, security, and industrial applications. These detectors directly convert X-rays into electrical signals, enabling low-dose operation while eliminating the need for scintillators. Artificial layered systems with high atomic number elements and favorable carrier transport properties such as perovskites, MXenes, and other 2D materials are particularly attractive due to their high X-ray sensitivity, ease of integration with conventional semiconductors, and compatibility to back-end-of-line (BEOL) CMOS process [1-6]. MXenes offer advantages over lead-based perovskites and other layered systems, as they can be synthesized free from hazardous and environmentally unstable elements [7, 8]. Their high electrical conductivity, excellent optical transparency, and solution processability make them suitable for large-scale image sensing [7]. In addition, the ability to tune their work function (1.6 to 6.2 eV) through surface modification allows for forming both Schottky and Ohmic contacts with various semiconductors [9]. Recent studies have explored MXene/semiconductor Schottky junctions, MXene/quantum dot heterojunctions, and MXene electrodes in perovskite devices for various photodetection applications [9-13].

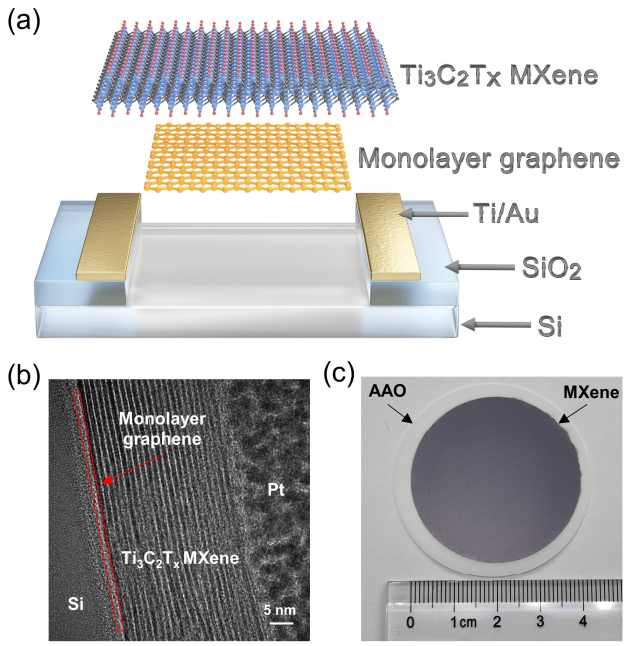

Fig.1 (a) The schematic diagram of the $Ti_3C_2T_x$ MXene/Graphene/Si device. (b) Cross-sectional AC-TEM image of $Ti_3C_2T_x$ MXene/Graphene/Si with protected Pt layer. (c) The photo of MXene nanofilm (2-inch) on AAO membrane.

Our previous work demonstrates the potential of van der Waals (vdW) integrated $Ti_3C_2T_x$ MXene nanofilms on silicon for ultrafast and sensitive X-ray detectors capable of producing X-ray images with limit of detection down to 2.85 $nGy_{air}\ s^{-1}$ [5]. In these detectors, the interface between the MXene and the bulk semiconductor is critical, fundamentally defining the performance and sensitivity. We observed that our $Ti_3C_2T_x$ MXene effectively absorbs X-rays and generates a large density of hot electrons suitable for photothermionic emission at the MXene/Si Schottky interface. In this study, we demonstrated significant suppression in dark current by two

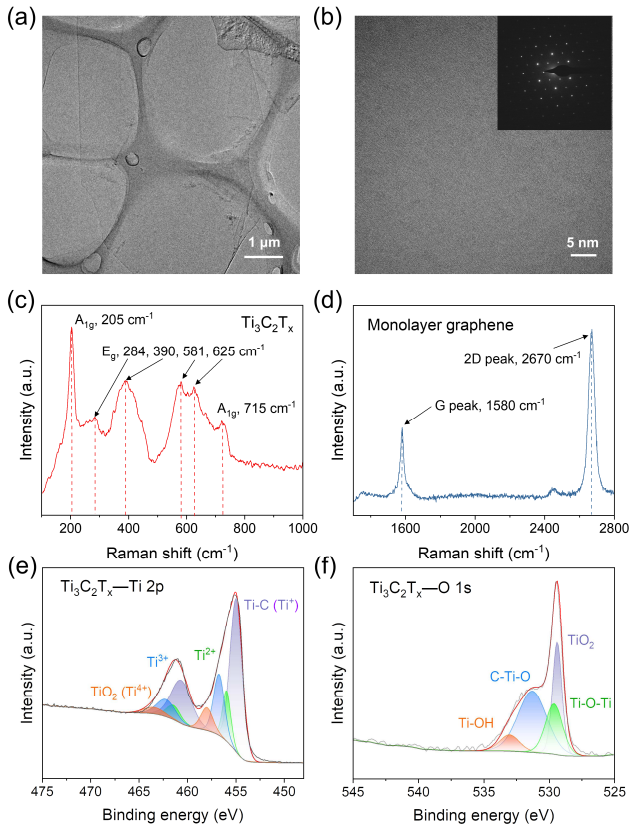

Fig.2 (a) TEM image of the $Ti_3C_2T_x$ flake. (b) AC-TEM image of $Ti_3C_2T_x$ flake. The inset showed the corresponding SAED pattern. (c) Raman spectrum of the $Ti_3C_2T_x$ MXene nanofilm. (d) Raman spectrum of the monolayer graphene. (e)-(f) XPS spectra of the $Ti_3C_2T_x$ MXene nanofilm (Ti 2p and O 1s core-level, respectively).

orders and improved X-ray sensitivity by 100% by inserting graphene interfacial layer at MXene/Si junction. This interfacial engineering approach offers a simpler alternative, avoiding the need for sophisticated deposition techniques typically used to create high-k dielectric and buffer layers for improved charge transfer at Schottky interfaces and improving photoinduced charge transfer that even reflects in the improved sensitivity of X-ray detection [14].

II. MXene/Si X-ray Detector with Graphene Interfacial Layer

A. Device Design and Fabrication

We fabricated two sets of $Ti_3C_2T_x$ MXene/Si heterojunctions, with and without graphene interfacial layer. A n-type silicon substrate with SiO_2 layer was first patterned via photolithography and then SiO_2 was selectively etched with buffer etchant to form Si windows. $Ti_3C_2T_x$ MXene nanofilm was prepared by vacuum filtration on an Anodic Aluminum Oxide (AAO) membrane. For the first set of samples, MXene nanofilm was directly transferred on silicon window (2 mm × 2 mm) using water-assisted peeling method described in our previous study [5]. For the second set of samples, a high-quality monolayer graphene was first transferred over the Si-window using a water-assisted method, followed by oxygen plasma etching and rapid thermal annealing (N_2 atmosphere, 400 °C, 5 min) to improve the quality of graphene-Si interface. Here, graphene was selectively pattered to confine within the Si window area. $Ti_3C_2T_x$ MXene layer was then transferred and patterned on this graphene/Si interface as shown in the schematic (Fig. 1a).

B. MXene/Graphene/Si Heterostructure

Fig. 1b shows the Aberration-Corrected transmission electron microscopy (AC-TEM) result of the cross-section of $Ti_3C_2T_x$ MXene/graphene/Si heterostructure. It reveals coherent bonding between the highly ordered $Ti_3C_2T_x$ MXene layer, monolayer graphene and silicon substrate. This atomically smooth heterointerface configuration enables efficient charge carrier transport. Fig. 1c shows a 2-inch-sized $Ti_3C_2T_x$ MXene nanofilm on an AAO membrane, which demonstrates a smooth and uniform surface morphology. Fig 2a displays the AC-TEM image of the $Ti_3C_2T_x$ flake with uniform surface. Fig. 2b exhibits a characteristic hexagonal arrangement of $Ti_3C_2T_x$ flake and its single crystallinity is further validated by the selected area electron diffraction (SAED) pattern in the inset of Fig. 2b. Shown in Fig. 2c, the significant Raman peaks of $Ti_3C_2T_x$ appeared at 201 and 715 cm^{-1}, corresponding to the A_{1g} vibration of Ti-C bonds. In Fig. 2d, the almost absent D peak (1350 cm^{-1}) indicated the structural integrity of the monolayer graphene and its ultra-low defect level. To confirm the composition and surface functional groups, X-ray photoelectron spectroscopy (XPS) was conducted to analyze the electronic states of the $Ti_3C_2T_x$ flake. Fig. 2e shows the Ti 2p core-level spectrum of $Ti_3C_2T_x$ flake, which is deconvoluted into four doublets (Ti $2p_{3/2}$, Ti $2p_{1/2}$) corresponding to Ti-C bonds (Ti^+), Ti^{2+}, Ti^{3+}, and TiO_2 (Ti^{4+}), respectively. In Fig. 2f, the O 1s core-level spectrum is fitted with four peaks which are attributed to TiO_2, Ti–O–Ti, C–Ti–O, and Ti–OH, respectively. The presence of oxygen and OH terminated groups lead to slight differences in Schottky barrier heights over the MXene-semiconductor interface. Here, adding a graphene layer presumably decouples the direct interaction between MXene and Si, thus providing a more uniform Schottky barrier over the entire Si-window.

III. X-ray Response and Imaging

A. X-ray Response Characteristics

Fig. 3a shows the schematic diagram of the system for testing X-ray response of the detectors. We employed an X-ray source (Mini-X2, Amptek) to irradiate the device, while using a digital Source Measure Unit (Model 2460, Tektronix Keithley) to apply bias voltage and record its current signal. Fig. 3b displays the I-V curves of $Ti_3C_2T_x$ MXene/graphene/Si (MXene/Gr/Si) and $Ti_3C_2T_x$ MXene/Si (MXene/Si) devices under dark conditions and X-ray irradiation (20 keV, 1.62 $\mu Gy_{air}\ s^{-1}$). Due to the incorporation of the high-quality monolayer graphene, the dark current of the MXene/Gr/Si device was reduced by nearly two orders of magnitude compared to the MXene/Si device, while the photocurrent was nearly twice that of the latter under identical conditions. Fig. 3c shows the photocurrent density of the MXene/Gr/Si device as a function of irradiation dose-rate under 10 keV and 20 keV X-ray exposure. The MXene/Gr/Si device exhibits a strong linear response, with the photocurrent density following the power law $J_{ph} \propto \alpha P^{\beta}$, where the fitted β values are 0.98 (10 keV), 1.01 (20 keV), and 0.999 (30 keV, in the inset). The MXene/Gr/Si device achieved a high sensitivity of 2.5×10^6 $\mu C\ Gy_{air}^{-1}\ cm^{-2}$ under 10 keV X-ray irradiation, while that of the MXene/Gr/Si was 1.2×10^6 $\mu C\ Gy_{air}^{-1}\ cm^{-2}$. In Fig. 3d, the MXene/Gr/Si device demonstrated a quite low noise

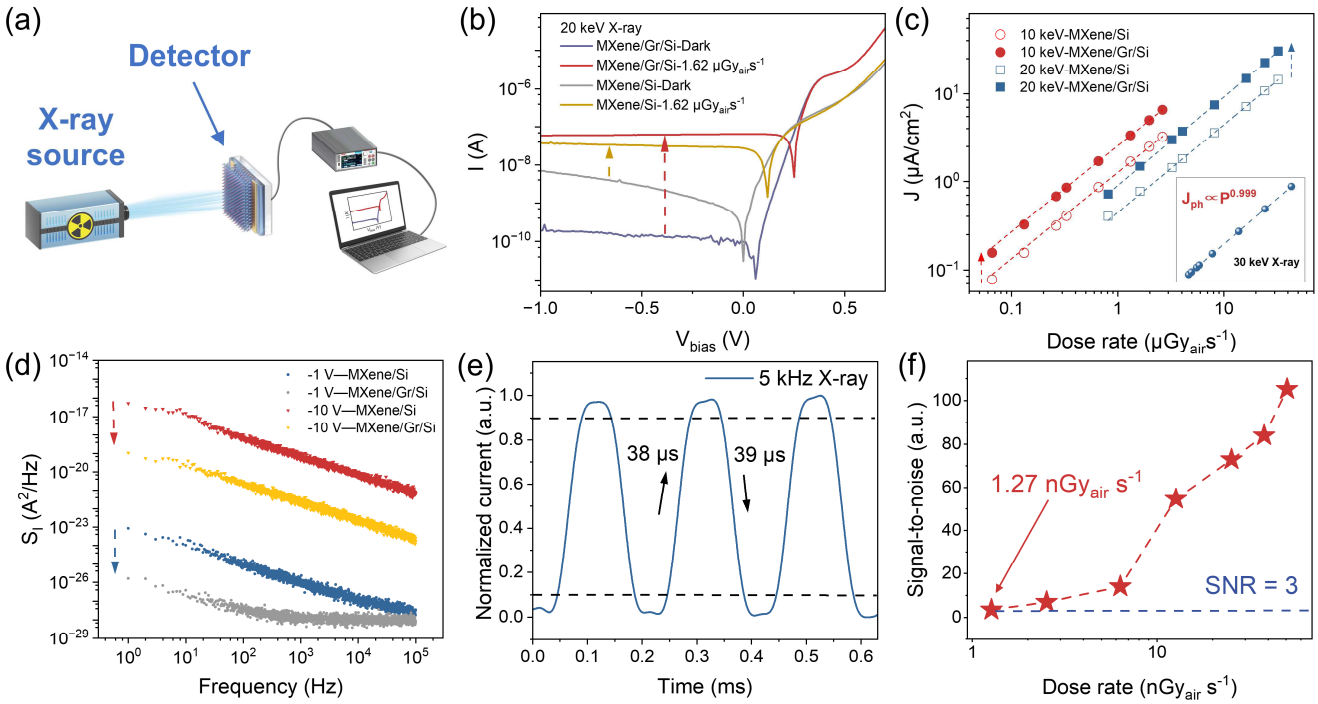

Fig.3 (a) The schematic diagram of the system for X-ray response test of the detectors. (b) The I–V curves of the MXene/Gr/Si and MXene/Si devices under dark condition and X-ray irradiation (photon energy: 20 keV). (c) Photocurrent density of the two kinds of devices as a function of dose rate under different X-ray photon energies at −1 V. The dash lines indicated the fitted linear curves. (d) Comparison of noise spectral density (NSD) between two kinds of devices under dark conditions at different bias voltages. (e) Measurement of X-ray response speed in MXene/Gr/Si detector (with signal frequency modulated by an optical chopper). (f) Dependence of the signal-to-noise ratio (SNR) on X-ray dose rate in the MXene/Gr/Si detector.

spectral density (NSD, S_I) three orders of magnitude lower than that of the MXene/Si device under both -1 V and -10 V, achieving a minimum value of 1.6×10^{-26} $A^2 \cdot Hz^{-1}$ (f = 1 Hz) at -1 V. To evaluate the X-ray response speed, the MXene/Gr/Si device was tested using an optical chopper to modulate X-ray signals, with an oscilloscope (MSO8104，RIGOL) for signal acquisition. As shown in Fig. 3e, the device exhibited rise and fall times of 38 μs and 39 μs under 5 kHz (maximum operating frequency of the chopper), respectively. However, the measured response time was constrained by the frequency limitation of the chopper and optical path delay in the measurement setup, while the intrinsic response time of the device is estimated to reach the tens of nanoseconds range [5]. The detection limit (LoD) serves as a key performance indicator for evaluating X-ray detectors in medical imaging applications. As illustrated in Fig. 3f, the MXene/Gr/Si detector achieved an LoD of 1.27 nGy_{air} s^{-1} at a signal-to-noise ratio (SNR) of 3, representing only 1/4330 of the dose required for conventional medical diagnostic procedures (5.5 μGy_{air} s^{-1}). This indicates the potential of vdW interfacial engineering with graphene to improve the sensitivity of X-ray detection in MXenes/ Si Schottky detector. Unlike other insulating interfacial layers used to passivate the MXene/Si interface and that increase the Schottky barrier height, a graphene interfacial layer provides a decoupled interface, preserving the original Schottky barrier height. This suppresses dark current while enhancing photo-thermionic emission of hot carriers generated during X-ray detection in MXenes.

B. Demonstration of X-ray Single-Pixel Imaging

Fig. 4a shows the X-ray single-pixel imaging system. An X-ray beam passes through an "X"-shaped sample and is then modulated by a 28×28-pixel stainless steel mask (252 patterns) positioned by a stepper motor. The modulated X-ray intensity is measured by the MXene/Gr/Si detector, and the final image is reconstructed using the iterative shrinkage-thresholding algorithm (ISTA). Shown in Fig. 4b, the image reconstruction process started with an N-pixel target image $x \in \mathbb{R}^N$ being modulated by Hadamard basis patterns $\Phi \in$

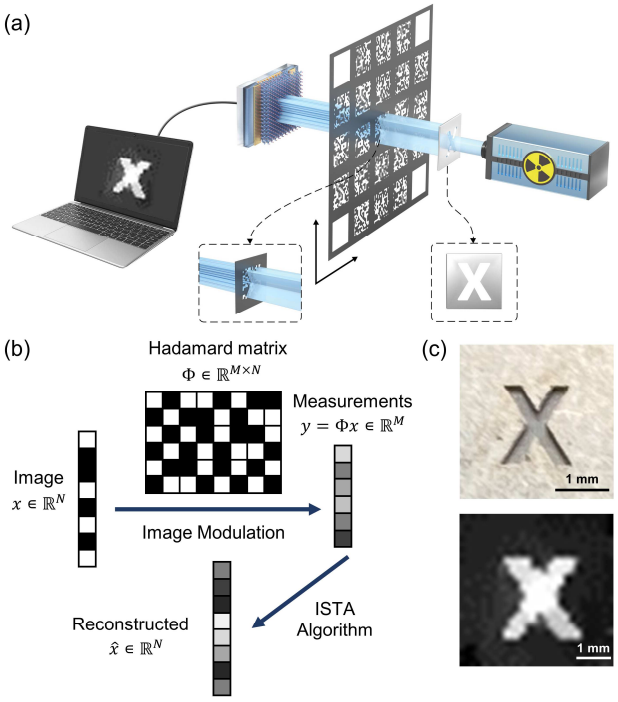

Fig.4 (a) The schematic diagram of the X-ray single-pixel imaging system. (b) The flow diagram of X-ray SPI. (c) The photo of the "X" letter sample and corresponding reconstructed image.

TABLE I. COMPARISON KEY PERFORMANCE METRICS IN X-RAY DETECTORS

	This Work	**Nat. Photonics [1]**	**Nat. Commun. [2]**	**Adv. Mater. [3]**	**Nat. Photonics [4]**
Material	$Ti_3C_2T_x$ MXene	MA PbI_3 film	$MAPbI_3$	$MA_{0.42}FA_{0.58}PbI_3$	2D layered $(NH_4)_3Bi_2I_9$
Thickness (μm)	0.33	300	400	70	1000
X-ray Energy (keV)	10-30	20-50	50	22	50
Bias (V)	-1	1	50	-5	10
Sensitivity ($\mu C\ Gy_{air}^{-1}\ cm^{-2}$)	2.5×10^6	2×10^3	2.24×10^4	1.16×10^6	8.2×10^3
LoD ($nGy_{air}\ s^{-1}$)	1.27	2.6	28.57	37.4	55
Response Time (ms)	<0.038	>1	<1000	2×10^4	80

$\mathbb{R}^{M\times N}$, producing measurement vectors $y = \Phi x \in \mathbb{R}^M$. Solving this underdetermined system requires addressing the inverse problem $y = \Phi x$ through regularized optimization. The ISTA was employed to address the optimization formulation: $\min_x g(x) + \lambda h(x)$ where $g(x) = \frac{1}{2}\|\Phi x - y\|_2^2$, with $h(x)$ defined as the total variation of image x. This algorithm computed the equation: $x^{(k)} = prox_{\lambda h}\left(x^{(k-1)} - \rho\Phi^T\left(\Phi x^{(k-1)} - y\right)\right), k \in \{1,2,\dots,n\}$ at k^{th} iteration where $prox_{\lambda h}(r) = arg\min_x \frac{1}{2}\|x - r\|_2^2 + \lambda h(x)$ and the final reconstructed image corresponds to $\hat{x} = x^{(n)}$. Fig. 4c shows the photo of the stainless steel "X" sample and the reconstructed image, demonstrating the high imaging resolution capability of this system. Table I compared the key performance metrics of the state-of-the-art X-ray detectors based on different photosensitive materials [1-4]. Our work outperforms in sensitivity, limit of detection, and response speed while maintaining compatibility with standard silicon processing, offering scalable integration potential for future X-ray detection and imaging technologies.

IV. Conclusion

This work demonstrates a highly sensitive $Ti_3C_2T_x$ MXene/Si X-ray detector enabled by graphene interfacial engineering, achieving enhanced performance in X-ray detection. By integrating monolayer graphene at the interface of $Ti_3C_2T_x$ MXene/Si heterojunction, the device exhibits a dark current reduction of two orders of magnitude and a photocurrent enhancement of 100% compared to MXene/Si counterparts, while maintaining exceptional linearity ($\beta \approx 1$) across 10–30 keV X-ray energies. The optimized heterostructure delivers a record sensitivity of 2.5×10^6 μC Gy_{air}^{-1} cm^{-2}, coupled with ultra-low noise spectral density (1.6×10^{-26} $A^2 \cdot Hz^{-1}$) and a sub-nGy detection limit (1.27 nGy_{air} s^{-1}), surpassing clinical requirements by 3 orders of magnitude. Further, the demonstrated single-pixel X-ray imaging system, leveraging Hadamard modulation and ISTA reconstruction, validates the capability of the MXene/Gr/Si device for high-resolution radiography with rapid response speed. This interfacial engineering strategy improves the X-ray detection sensitivity while demonstrating a scalable framework for advanced imaging systems. Combining the excellent photo-response properties of 2D materials with the mature fabrication processes of silicon, this work opens avenues for next-generation low-dose, high-speed medical and industrial imaging technologies.

Acknowledgment

This work is supported by the National Key Research and Development Program of China (2022YFA1204304), Zhejiang Technology Innovation Center of CMOS IC Manufacturing Process and Design, the start-up funding of ZJU-HIC Centre (04010000-K02013007).

References

[1] K. Sakhatskyi, B. Turedi, G. J. Matt *et al.*, "Stable perovskite single-crystal X-ray imaging detectors with single-photon sensitivity," Nature Photonics, vol. 17, no. 6, pp. 510-517, 2023.

[2] Z. Song, X. Du, X. He *et al.*, "Rheological engineering of perovskite suspension toward high-resolution X-ray flat-panel detector," Nature Communications, vol. 14, no. 1, p. 6865, 2023.

[3] W. G. Li, X. D. Wang, Y. H. Huang *et al.*, "Ultrasound-assisted crystallization enables large-area perovskite quasi-monocrystalline film for high-sensitive X-ray detection and imaging," Advanced Materials, vol. 35, no. 31, p. 2210878, 2023.

[4] R. Zhuang, X. Wang, W. Ma *et al.*, "Highly sensitive X-ray detector made of layered perovskite-like $(NH_4)_3Bi_2I_9$ single crystal with anisotropic response," Nature Photonics, vol. 13, no. 9, pp. 602-608, 2019.

[5] Y. Chen, Y. Dai, S. C. Bodepudi *et al.*, "High-sensitive and fast MXene/silicon photodetector for single-pixel X-ray imaging," InfoMat, vol. 6, no. 9, p. e12596, 2024.

[6] B. Hou, Q. Chen, L. Yi *et al.*, "Materials innovation and electrical engineering in X-ray detection," Nature Reviews Electrical Engineering, vol. 1, no. 10, pp. 639-655, 2024.

[7] A. VahidMohammadi, J. Rosen, and Y. Gogotsi, "The world of two-dimensional carbides and nitrides (MXenes)," Science, vol. 372, no. 6547, p. eabf1581, 2021.

[8] K. R. G. Lim, M. Shekhirev, B. C. Wyatt *et al.*, "Fundamentals of MXene synthesis," Nature Synthesis, vol. 1, no. 8, pp. 601-614, 2022.

[9] A. Agresti, A. Pazniak, S. Pescetelli *et al.*, "Titanium-carbide MXenes for work function and interface engineering in perovskite solar cells," Nature materials, vol. 18, no. 11, pp. 1228-1234, 2019.

[10] Y. Zheng, Y. Wang, Z. Li *et al.*, "MXene quantum dots/perovskite heterostructure enabling highly specific ultraviolet detection for skin prevention," Matter, vol. 6, no. 2, pp. 506-520, 2023.

[11] Y. Sun, Z. Liu, Y. Ding *et al.*, "Flexible broadband photodetectors enabled by MXene/PbS quantum dots hybrid structure," IEEE Electron Device Letters, vol. 42, no. 12, pp. 1814-1817, 2021.

[12] Y. Di, K. Ba, Y. Chen *et al.*, "Interface engineering to drive high - performance MXene/PbS quantum dot NIR photodiode," Advanced Science, vol. 11, no. 6, p. 2307169, 2024.

[13] L. Li and G. Shen, "MXene based flexible photodetectors: progress, challenges, and opportunities," Materials Horizons, vol. 10, no. 12, pp. 5457-5473, 2023.

[14] Z. Liu, M. Li, Z. Liu *et al.*, "Heterostructured MXene/Si photodiodes with sub-1-nm h-BN blocking layers for suppressing dark current," IEEE Electron Device Letters, vol. 44, no. 3, pp. 476-479,